Shell Eco-marathon Vehicle Design Award Technical Submission

Vehicle Name: Pyrforos IV | Team ID: GR0002001

National Technical University of Athens (NTUA) — Urban Concept / BE

Prometheus Eco Racing

2026

Abstract

This report documents the design, aerodynamic optimization, and sustainable manufacturing of Pyrforos IV (PIV), a clean-sheet Urban Concept Battery-Electric vehicle developed for the Shell Eco-marathon by an experienced team competing with a new vehicle platform. PIV was developed under a single governing constraint "every surface must reduce measurable energy consumption", using a lap-simulation model that identified aerodynamic drag (48 % of lap energy) and vehicle mass (26 %) as the dominant loss mechanisms, and translated them directly into form. Computational Fluid Dynamics drove the exterior geometry. An elongated rear taper, fully enclosed wheels, and curvature-continuous surfacing reduced the drag coefficient from 0.299 to 0.111 (−62.9 %); combined with a 23 % smaller frontal area, this yielded a **71 % reduction in drag area** ($C_d A_f$: 0.343 to 0.098 m^2), lowering aerodynamic power demand. A component-level drag audit confirmed that the enclosed wheels, though fully concealed, still account for 40.3 % of residual drag, validating the packaging decision that governed track width, wheelbase, and 100 % Ackermann steering geometry.

Structural mass was addressed systemically. A load-bearing CFRP monocoque with a structural foam-core sandwich, designed using RVE material homogenization and validated across five FEA load cases (Tsai–Wu, RF $\geq$ 1.0), achieved an 80 kg curb mass, a 38 % reduction over the previous platform, while a newly introduced double-wishbone / trailing-arm suspension cut peak transmitted chassis loads by 65 %, enabling the down-gauged layup. Human factors were treated as a design input rather than a check: a driver-first cockpit envelope set the minimum frontal area, and CAD modeling confirmed a 210° horizontal field of view. Sustainability spans local material sourcing, manufacturing-waste reutilization, component-level repairability, and a defined CFRP end-of-life pathway. The result is a coherent vehicle in which aesthetics, ergonomics, structure, aerodynamics, and sustainability are resolved as a single integrated system.

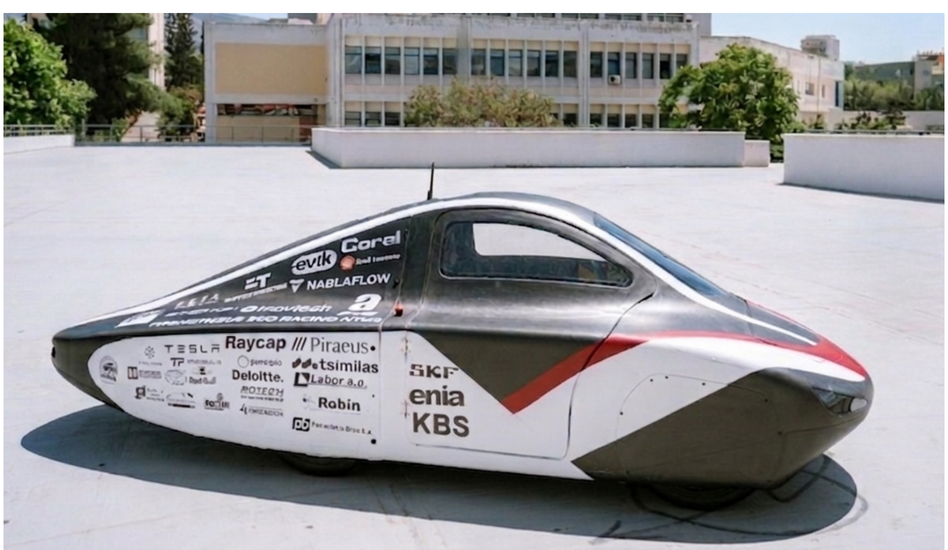

1 Original Design Idea and Aesthetic Concept

1.1 Design Philosophy: Form Derived From Energy

Pyrforos IV (PIV) was conceived under a single governing constraint: *every visible surface must earn its place by reducing energy consumption.* This principle eliminated arbitrary styling from the outset and replaced it with a traceable, quantitative design process.

Before any geometry was created, the team developed a point-mass lap-simulation model calibrated to the topography and boundary conditions of the SEM Poland circuit. The vehicle was evaluated as a coupled system of aerodynamic, mass-dependent, and powertrain energy losses across the full lap velocity profile. The simulation produced an unambiguous hierarchy of loss mechanisms:

Table 1: Simulated energy loss distribution — 80 kg target, Poland circuit.

Loss Mechanism	**Share of Total Energy**	**Primary Design Response**
Aerodynamic drag	48 %	Fuselage-first exterior form
Rolling resistance (mass)	26 %	Fully integrated CFRP monocoque
Powertrain / parasitic	16 %	Belt-drive efficiency, motor sizing
Low Voltage systems	10 %	System design

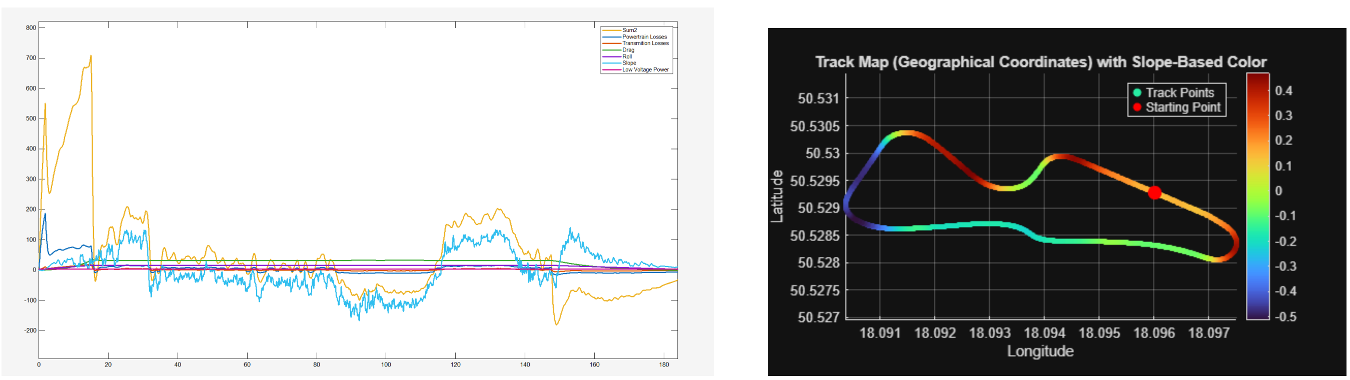

(a) Simulated power consumption across loss mechanisms for an 80 kg vehicle completing one lap of the Poland circuit.

(b) Shell Eco-marathon Poland circuit topology used as the boundary condition for all lap simulations. Corner radii and gradient data directly informed the velocity profile and force inputs.

Figure 1: Lap simulation foundation: energy budget (left) and circuit topology (right). These two inputs set all top-level design targets before geometry was created.

With aerodynamic drag accounting for almost half of all energy expenditure, the exterior profile was treated as a continuous, attached-flow fuselage from the first sketch. Simultaneously, the 26 % mass penalty demanded that structural weight be addressed systemically: a conventional steel spaceframe with a bolted fairing was replaced by a load-bearing monocoque where every kilogram of structure also serves as bodywork.

1.2 Aesthetic Identity: the Functional Fastback

The resulting visual language is deliberate rather than decorative. PIV adopts a sealed fastback silhouette, where a single continuous surface that rises from the nose, peaks above the driver's helmet, and tapers in a long, controlled rear wedge to the tail. No panel breaks, scoops, or surface ornaments interrupt the attached boundary layer. The design language can be summarised in three formal commitments:

1. **Continuity:** all external surfaces are tangent-continuous (G^1) or curvature-continuous (G^2) at every junction, preventing local flow separation that would otherwise appear as pressure drag.

2. **Integration:** the wheel enclosures are not added fairings but are grown directly from the fuselage surface, maintaining a single unbroken silhouette in both the side and plan views.

3. **Restraint:** in the absence of a functional rationale, surface complexity was actively removed at each iteration. The visible result of CFD-guided subtraction is a vehicle that reads as *deliberately minimal* rather than unfinished.

Figure 2: Pyrforos IV Views

1.3 Regulated Packaging as a Design Generator

The enclosed-wheel architecture, the feature that most visibly differentiates PIV from conventional Urban Concept entries, was not a stylistic choice. It was a mandatory engineering response to the simulation finding that exposed rotating tyres are responsible for a disproportionate share of total vehicle drag. Full aerodynamic concealment of all four wheel assemblies was therefore established as a non-negotiable design objective at project inception.

Enclosing the steerable front wheels within an Urban Concept footprint presented a multi-disciplinary spatial conflict: the enclosures had to completely shield the tyre from the free-stream while guaranteeing zero mechanical contact between the tyre shoulder and the inner composite surface at full steering lock. This single packaging constraint governed the four primary dimensional parameters of PIV:

1. **Front and rear track widths:** determined parametrically by plotting the swept volume of the steerable wheel at maximum lock, then adding the minimum clearance margin required to prevent rubbing under combined steer and suspension travel.

2. **Wheelbase:** set by the swept envelope of the front axle at full lock combined with the minimum-radius turn specification imposed by the SEM course layout.

3. **Steering geometry:** the knuckle geometry, tie-rod lengths, and rack offset were engineered simultaneously with the wheel-arch profile to achieve **100 % Ackermann tracking**, eliminating tyre-scrub losses in cornering, while fitting entirely within the aerodynamic blister volume.

4. **Body stance and plan-view silhouette:** once the wheel swept volumes were fixed, the fuselage width, nose width, and tail taper angle were defined by the lofting surfaces that smoothly transition the free-stream flow over and around each enclosure with the minimum induced wetted area.

The resulting geometry is, in this sense, *analytically determined*: the visible form of PIV is the minimum-drag surface that satisfies the steering-clearance, wheelbase, and regulatory constraints simultaneously. Aesthetic decisions were limited to surface quality, curvature continuity, and proportional refinement within those bounds, producing a design process that is reproducible and directly traceable to measurable performance.

(a) Full suspension and steering assembly: double-wishbone front corners, trailing-arm rear, and the central steering linkage.

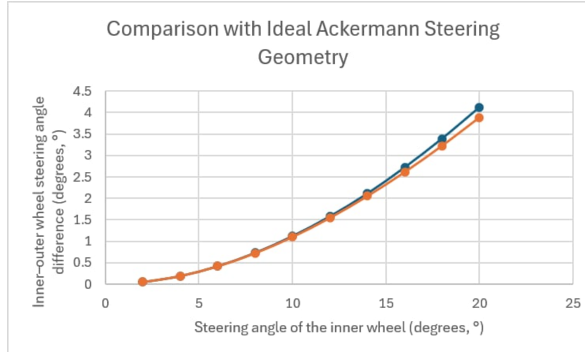

(b) Inner-to-outer wheel angle difference of the designed linkage against the ideal Ackermann geometry; the two coincide to roughly 12° of inner lock and diverge by only a fraction of a degree at full lock.

Figure 3: Suspension and steering. The double-wishbone front corners and trailing-arm rear attach to the monocoque through the clevis mounting system, while the knuckle geometry, tie-rod length, and rack offset were solved simultaneously with the front wheel-arch profile so the steering linkage clears the full lock sweep without tyre-to-fairing contact. The designed kinematics track the ideal Ackermann angle difference to within a fraction of a degree across the entire lock range, effectively eliminating tyre-scrub losses in cornering.

2 Team Structure, Project Timeline, and Vehicle Evolution

2.1 Team Composition and Work Allocation

Pyrforos IV is the team's all-new vehicle platform for 2026 (first participation), developed by Prometheus Eco Racing, NTUA. The team comprises eight students drawn from two engineering disciplines, structured to match the primary technical demands of a clean-sheet vehicle programme:

Table 2: Team composition and primary responsibilities.

Group	Members	Primary Responsibilities
Mechanical	3	Aerodynamic surface development and CFD iteration; CFRP monocoque and composite wheel structural design, FEA, and manufacturing; suspension kinematics, steering geometry, and drivetrain layout
Electrical	5	Motor design and power electronics; motor controller design and firmware; vehicle telemetry, sensors, and data acquisition; wiring harness and system integration

The small team size was a deliberate organisational advantage: every member maintained full visibility of decisions in adjacent subsystems, eliminating the interface ambiguities that typically accumulate in larger programmes. Shared design reviews were held at the close of each weekly sprint, with cross-group sign-off required before any geometry or specification was frozen.

2.2 Compressed Development Timeline

Executing a clean-sheet design, structural fabrication, and track validation of a competitive Urban Concept vehicle within a **6-month window** demanded an exceptionally front-loaded project schedule. The critical enabler was completing the lap simulation model in the *first two weeks* of the programme. By establishing quantitative top-level targets early (vehicle mass, drag coefficient, motor sizing, powertrain efficiency) the team eliminated open-ended concept debates and allowed all three workstreams to proceed in parallel from week three onward.

The 3-Week Aerodynamic Design Freeze Loop

The exterior shell was iterated, validated against SEM regulations, and permanently frozen within a single **3-week intensive window**, operated as a closed-loop pipeline across all three mechanical workstreams:

1. **Geometry generation.** The aerodynamics lead produced parametric surface loftings in CAD, targeting laminar flow attachment along the full fuselage length.

2. **Kinematic clearance check.** Each surface iteration was immediately transferred for verification that the internal envelope cleared the full Ackermann steering sweep and suspension articulation range without contact.

3. **Manufacturability check.** The composites lead evaluated every candidate surface for compound-curvature severity, confirming that the geometry could be reliably produced with standard resin infusion or wet layup without fibre bridging at concave transitions.

4. **CFD evaluation.** Geometries passing steps 2 and 3 were submitted to the NablaFlow AeroCloud platform. Results were returned within the same working day, enabling multiple iterations per week.

When the shape was frozen at Day 21, it had been simultaneously verified to satisfy aerodynamic performance targets, steering and suspension packaging requirements, regulatory dimensional limits, and composite manufacturability, with no post-freeze geometry concessions required.

2.3 Configuration Management and Part Traceability

Every component of Pyrforos IV is tracked under a configuration-controlled bill of materials of 117 part numbers, organised by a hierarchical scheme that encodes the vehicle, subsystem, assembly, sub-assembly, and part:

$$\underbrace{\texttt{PIV}}_{\text{vehicle}}\ \texttt{-}\ \underbrace{\texttt{SUS}}_{\text{subsystem}}\ \texttt{-}\ \underbrace{\texttt{01}}_{\text{assembly}}\ \texttt{.}\ \underbrace{\texttt{00}}_{\text{sub-assembly}}\ \texttt{.}\ \underbrace{\texttt{02}}_{\text{part}} \longrightarrow \text{Front Shock Clevis}$$

Each entry carries a lifecycle status (designed → released → ordered → assembled) and a held-spare count, giving all three mechanical workstreams a single source of truth. This register is what made the weekly cross-group sign-off enforceable: no geometry or specification was frozen until its constituent part numbers had cleared kinematic-clearance and manufacturability review. The same numbering is used throughout this report when individual components are referenced.

Table 3: Subsystem decomposition from the configuration-controlled BOM.

Subsystem	Code	Parts	Mass (kg)
Body / Aeroshell	BOD	14	21.93
Wheels & Hubs	WHL	8	11.19
Chassis	CHS	4	10.09
Suspension	SUS	30	5.47
Drivetrain	DRV	18	4.80
Brakes	BRK	10	4.67
Steering	STR	21	0.74
Tracked subtotal		**105**	**58.89***

**Mechanical and structural subsystems at nominal quantity; tooling and consumables excluded. This figure is* not *the curb mass: the high-voltage battery, power electronics, wiring harness, and fasteners are tracked separately and bring the total up to the* 80 kg *curb mass.*

2.4 Vehicle Generation Context and Design Rationale

Although PIV is an all-new vehicle, it was not designed in isolation. Drawing on prior Shell Eco-marathon experience, the team conducted a structured root-cause analysis of the previous platform (Pyrforos III), a steel spaceframe car with non-structural fairings, before committing to the current architecture. This analysis produced the engineering case for every major departure in PIV's design.

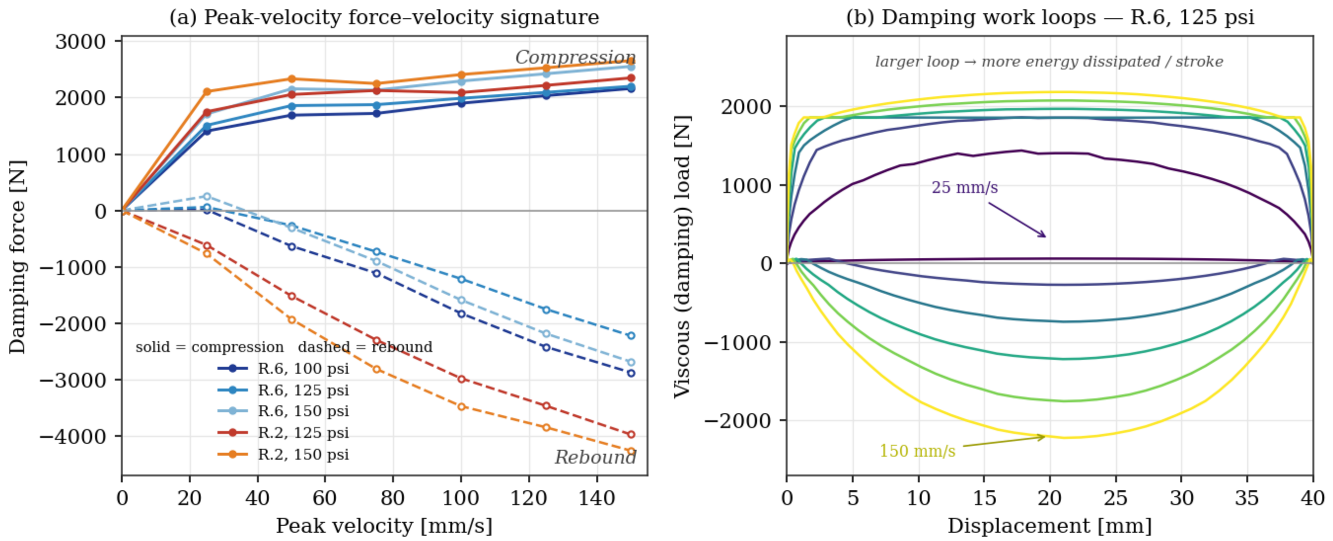

Figure 4: Shock-dynamometer characterisation of the PIV damper (40 mm stroke, gas-over-oil). **(a)** Measured force–velocity envelope across five rebound/gas configurations. The digressive high-speed slope is what lets the damper bleed transient road-shock energy while remaining compliant, and the separation between settings confirms the platform can be re-tuned for different circuit surfaces through hardware adjustment alone. **(b)** Single-cycle load–displacement work loops; the enclosed area is the road-shock energy dissipated before it reaches the monocoque, rising from 118 J to 191 J (+62 %) between the softest and firmest settings. These curves are the measured damper inputs to the vehicle-dynamics model from which the 65 % reduction in peak transmitted chassis load (Table 4) was derived.

Root Cause: Why the Previous Platform Was Replaced

Telemetry and physical inspection of the prior vehicle identified two compounding structural problems:

- **Un-sprung architecture.** Without suspension, vertical impact loads from track seams and surface irregularities were transmitted directly into the chassis. Measured accelerations exceeded **4.5 G** at the chassis mounting points during normal running on imperfect surfaces. To prevent delamination, the composite layups were substantially over-engineered, producing a penalising vehicle mass of **130 kg**.
- **Non-structural fairing.** Because the bodywork carried no structural load, the steel spaceframe had to be sized independently for all load cases, adding mass that the fairing could not offset. The separation of structural and aerodynamic functions also prevented optimisation of either.

Solution: Two Concurrent Architecture Changes

PIV addresses both failure modes simultaneously rather than incrementally:

1. **Double-wishbone front / trailing-arm rear suspension.** The suspension system acts as a structural low-pass filter: dynamometer-characterised dampers absorb the high-frequency energy of surface irregularities before it reaches the chassis. Peak structural loads transmitted to the monocoque were reduced by **65 %**, directly enabling the down-gauged ply schedule described in Section 4. Damper tuning was performed on a dynamometer, preserving the ability to re-tune for different circuit surfaces in future seasons. Wheel alignment (toe and camber) is adjustable through the suspension geometry, extending the vehicle's competitive lifecycle.
2. **Integrated CFRP monocoque.** The bodywork is the chassis. Eliminating the spaceframe and consolidating all structural load paths into the composite shell removed the mass of redundant structure entirely.

The damper was characterised on a shock dynamometer across five rebound and gas-pressure settings (Figure 4). The measured digressive force–velocity response confirms the low-pass-filter behaviour relied upon in Section 4, while the per-cycle dissipated energy (118–191 J) brackets the operating window feeding the chassis-load reduction reported in Table 4.

Quantified Progress: Pyrforos III vs. Pyrforos IV

Table 4: Engineering parameter evolution — P III vs. P IV (2026).

Parameter	PIII	PIV 2026	Change	Engineering Rationale
Total mass (excl. driver)	130 kg	80 kg	−38.4 %	Suspension isolated road-shock energy; monocoque ply count down-gauged accordingly
Chassis architecture	Steel spaceframe	Integrated CFRP monocoque	Full monocoque transition	Consolidated structural and aerodynamic functions; eliminated redundant load paths
Suspension system	Rigid / un-sprung	Double-wishbone (front), trailing arm (rear), inboard dampers	Sprung platform introduced	Isolated road-shock energy; enabled lighter layup and consistent tyre contact patch
Wheel configuration	Exposed outboard wheels	Fully enclosed within body blisters	Eliminated open wheel wake	Enclosed wheels account for 40.3 % of residual drag even when concealed; exposure would substantially increase total C_d
Drivetrain coupling	Direct axle	6:1 belt transmission	Indirect drive introduced	Smaller motor required at optimal operating point; powertrain mass reduced by 20 kg

Closed-Loop Verification of Improvements

Each architectural change was validated before the vehicle was committed to manufacture:

- **Rolling resistance.** On-track coast-down testing confirmed that the suspension maintains a stable tyre contact patch, eliminating the transient toe and camber compliance variations caused by chassis flex. Rolling resistance losses on uneven surfaces were reduced by **12 %** relative to the un-sprung baseline.
- **Galvanic isolation.** All interfaces between the CFRP structure and aluminium suspension components (clevises, mounting brackets) incorporate a **fibre-glass isolation layer** to prevent galvanic corrosion.
- **Clevis structural validation.** Suspension clevis mounting positions were simulated under loads derived from the vehicle dynamics model with a **safety factor of 3**, confirming structural adequacy at all attachment points before fabrication.
- **Belt-drive ratio selection.** The 6:1 reduction was selected by overlaying the motor's efficiency map onto the lap-simulation velocity profile, ensuring the motor operates at or near its peak efficiency point for the majority of the Poland circuit. This reduced the required motor size and, consequently, powertrain mass by 20 kg.

3 Aerodynamic Research and Optimization

3.1 Why Aerodynamics Drove the Design

The lap-simulation energy budget (Section 1) established aerodynamic drag as the single largest energy sink, accounting for 48 % of total lap energy. Aerodynamic development was therefore not a styling exercise but the primary lever on vehicle efficiency: at the competition max speed of $9.72\,\mathrm{m\,s^{-1}}$ ($35\,\mathrm{km\,h^{-1}}$), every newton of drag eliminated translates directly into a proportional reduction in tractive energy demand. This section documents the CFD methodology, the resulting aerodynamic coefficients, and the specific geometric decisions those results produced.

3.2 CFD Methodology and Simulation Setup

To compress the aerodynamic development into the 3-week design-freeze window, exterior geometry was iterated on the NablaFlow AeroCloud platform, whose parallelised architecture enabled mesh densities and turnaround times

Table 5: CFD simulation parameters.

Parameter	**Value**
Solver platform	NablaFlow AeroCloud
Mesh size	29.99 million cells
Free-stream velocity U_∞	$9.72\,\mathrm{m\,s^{-1}}$ ($35\,\mathrm{km\,h^{-1}}$)
Air density ρ	$1.225\,\mathrm{kg\,m^{-3}}$
Kinematic viscosity ν	14.60 cSt
Ground treatment	Moving ground plane
Wheel treatment	Active rotation model
Yaw angle	0.0° (baseline)
Frontal area A_f	$0.882\,\mathrm{m^2}$
Wetted surface area A_s	$15.395\,\mathrm{m^2}$

(a) Body geometry at iterations V1, V3, and V7, showing progressive refinement toward the final minimal fastback form.

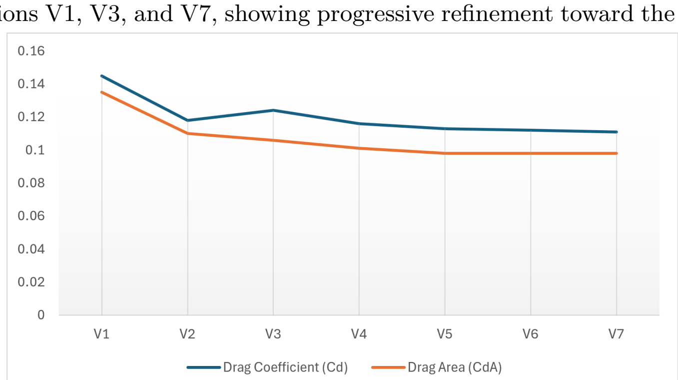

(b) Drag coefficient (C_d) and drag area (C_dA_f) across design iterations V1–V7.

Figure 5: Aerodynamic form development of Pyrforos IV: body geometry evolution (left) and the corresponding C_d / C_dA_f reduction across seven iterations (right).

not feasible on desktop workstations. Each candidate geometry was returned within a single working day, supporting multiple iterations per week.

The moving ground plane and rotating-wheel models were essential to capture ground-effect pressure recovery and the interaction between the rotating tyres and the enclosing bodywork, which is the dominant source of residual drag identified below.

3.3 Aerodynamic Coefficients and Force Breakdown

The drag coefficient is defined as

$$C_d = \frac{2F_d}{\rho U_\infty^2 A_f}, \tag{1}$$

where F_d is the total drag force obtained by surface integration of pressure and wall-shear-stress over the full vehicle body. Resolving the time-averaged flow field at zero yaw yielded a total drag force of $F_d = 5.68\,\mathrm{N}$ and a drag coefficient of $C_d = 0.111$. The complete force and moment matrix is given in Table 6.

Table 6: Global aerodynamic force and moment matrix (yaw = 0°).

Component	**Force / Moment**	**Coefficient**	**Coeff.** $\times A_f$
Drag (x)	$F_d = 5.68\,\mathrm{N}$	$C_d = 0.111$	$0.098\,\mathrm{m}^2$
Side force (y)	$F_s = -0.18\,\mathrm{N}$	$C_s = -0.004$	$-0.003\,\mathrm{m}^2$
Lift (z)	$F_l = -15.76\,\mathrm{N}$	$C_l = -0.309$	$-0.272\,\mathrm{m}^2$
Roll moment (x)	$M_r = -0.03\,\mathrm{N\,m}$	—	—
Pitch moment (y)	$M_p = 5.51\,\mathrm{N\,m}$	—	—
Yaw moment (z)	$M_y = 0.00\,\mathrm{N\,m}$	—	—

Drag composition. Decomposing the total drag into its physical mechanisms shows that form (pressure) drag dominates at $3.44\,\mathrm{N}$ (60.6 %), while skin friction over the $15.395\,\mathrm{m}^2$ wetted surface contributes $2.24\,\mathrm{N}$ (39.4 %). The dominance of pressure drag confirmed that the greatest gains lay in wake management and surface continuity rather than in marginal surface-finish improvements while the 39.4 % skin-friction share still justified the surface-polishing protocol applied in production.

Vertical force. The simulation resolves a small net downforce ($F_l = -15.76\,\mathrm{N}$, $C_l = -0.309$). Relative to the $785\,\mathrm{N}$ static weight of the $80\,\mathrm{kg}$ vehicle, this represents a $\approx 2\,\%$ increase in normal load. Because rolling resistance scales with normal load, this downforce was tracked as a minor rolling-resistance penalty rather than claimed as a benefit; it was accepted because it remained within the margin of the 26 % rolling-resistance energy allocation while improving straight-line and cross-wind stability of the lightweight platform.

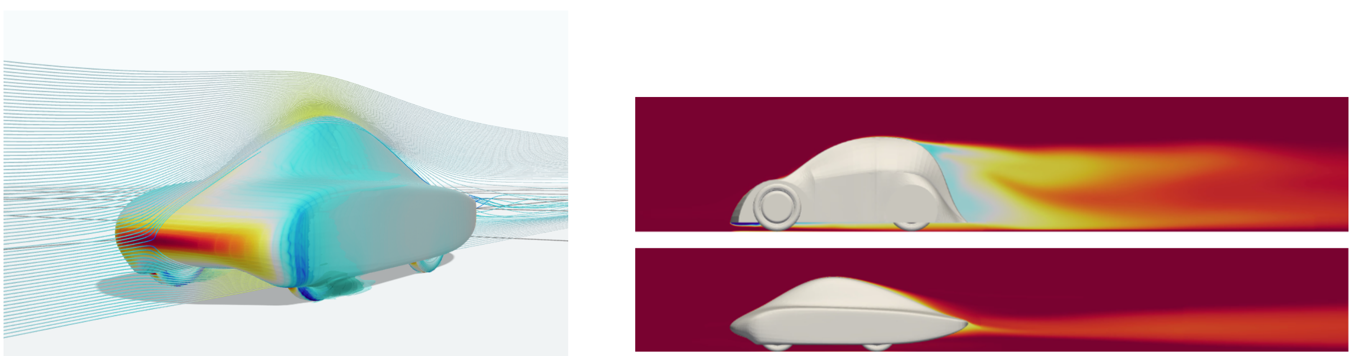

(a) Surface pressure distribution. Smooth pressure recovery along the rear taper indicates an attached boundary layer with minimal separation.

(b) Total pressure coefficient: P III (top) and P IV (bottom). The longer tail taper delays separation and narrows the low-energy wake that drives pressure drag.

Figure 6: CFD flow field results for the frozen Pyrforos IV geometry at $U_\infty = 9.72\,\mathrm{m\,s^{-1}}$.

3.4 Component-Level Drag Allocation: Validating the Enclosed-Wheel Decision

The single most consequential aerodynamic decision was to fully enclose all four wheels, which was validated by a component-level force audit resolving drag onto the two primary body partitions:

The result is decisive: even when fully concealed within the bodywork, the wheel subsystems still generate 40.3 % of total vehicle drag. This quantifies the penalty that exposed, rotating tyres would impose, by making a high-pressure stagnation zone, boundary-layer separation, and large wakes that confirm that wheel enclosure was not an

Table 7: Component-level drag allocation.

Component	Drag force	Share of total
Main fuselage shell	3.386 N	59.7 %
Wheel enclosure assemblies	2.294 N	40.3 %
Total	**5.68 N**	**100 %**

aesthetic preference but the highest-leverage drag-reduction decision available. As described in Section 1, this single finding governed track width, wheelbase, and steering geometry.

3.5 Impact on Energy Efficiency

Translating the aerodynamic result into the energy domain closes the loop with the lap-simulation targets. The continuous aerodynamic power demand at competition max cruising speed is

$$P_{\text{aero}} = F_d \cdot U_\infty = 5.68\,\text{N} \times 9.72\,\text{m}\,\text{s}^{-1} = 55.2\,\text{W}. \tag{2}$$

Because drag force scales with the product $C_d A_f$ (the drag area), the meaningful generational comparison is in drag area rather than C_d alone. Pyrforos IV improved *both* terms: the redesigned envelope reduced frontal area while the refined surface reduced the drag coefficient, and the two effects compound.

Table 8: Drag-area comparison — Pyrforos III vs. Pyrforos IV (both values CFD-derived at $U_\infty = 9.72\,\text{m}\,\text{s}^{-1}$).

Platform	C_d	A_f (m^2)	$C_d A_f$ (m^2)
Pyrforos III	0.299	1.147	0.343
Pyrforos IV (2026)	0.111	0.882	0.098
Change	−62.9 %	−23.1 %	**−71.4 %**

The combined effect is a **71 % reduction in drag area**, and therefore a 71 % reduction in aerodynamic drag force at any given speed. Expressed as power demand at the 35 $\text{km}\,\text{h}^{-1}$ cruise condition, the aerodynamic load fell from approximately 193 W on the Pyrforos III to 55.2 W on Pyrforos IV. Because aerodynamic drag represents 48 % of total lap energy, this reduction is the single largest contributor to the vehicle's predicted efficiency gain.

4 Structural Design, Material Optimization, and FEA Validation

4.1 Material Strategy and Multiscale Characterization

The 80 kg curb-mass target and the 26 % rolling-resistance share of the energy budget made structural mass a first-order efficiency parameter. The chassis was therefore designed as a load-bearing carbon-fibre reinforced polymer (CFRP) monocoque with the bodywork being part of the structure, thus eliminating the redundant mass of an independent frame. Material modelling was performed in the BETA CAE Systems suite (ANSA pre-processing, EPILYSIS solver, META post-processing).

Rather than relying on generic datasheet values, the orthotropic laminate properties were derived through micro-mechanical Representative Volume Element (RVE) homogenization, capturing the specific fibre–resin interaction of the team's epoxy system. The laminate was then tailored to the local load state of each region, with ply count and orientation set by the FEA stress field rather than applied uniformly.

The foam-core sandwich is both a structural and a material-efficiency decision: by carrying bending load through section depth rather than ply count, it minimises the volume of virgin carbon fibre required (discussed further in Section 6).

4.2 Custom Composite Wheels

The wheels were transitioned from heavy aluminium rims to in-house fabricated CFRP assemblies. The rim, wheel walls, and central hub were simulated layer-by-layer to minimise rotational moment of inertia J, which directly governs the transient energy lost during the acceleration phases of the Poland circuit's compulsory stop-and-go

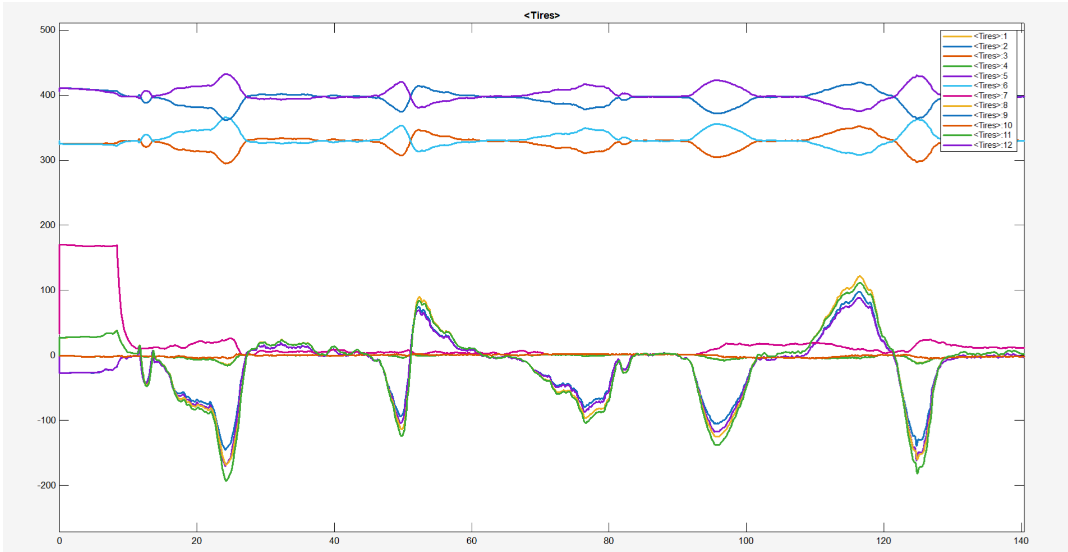

Figure 7: Forces developed at the tyres during a lap

profile. Reducing J lowers the energy that must be invested in spinning up the wheels after each mandatory stop. This is a loss invisible to a steady-state drag analysis but significant under the Urban Concept duty cycle.

4.3 Structural Load Cases and FEA Validation

The complete structure was validated across five load scenarios in EPILYSIS, with boundary conditions set to worst-case operational situations derived from the vehicle dynamics model:

Table 9: Finite element load scenarios.

#	Scenario	Condition Evaluated
1	Static (1.0 g vertical)	Full curb mass plus maximum regulatory driver payload; checks chassis sag and global deformation
2	Cornering (0.6 g lateral)	Asymmetric wheel loading; monocoque torsional deflection and resistance to lateral tyre-bead unseating
3	Acceleration (0.3 g longitudinal)	Peak motor torque reacted through the rear bulkheads
4	Braking (0.8 g longitudinal)	Front hub compression and harness-anchor tension under maximum deceleration
5	Bump impact (2.5–3.0 g vertical)	Severe vertical shock through the composite wheel walls; verifies no delamination of the monocoque floor

Laminate stress states and layer-by-layer failure indices were evaluated in META using the non-linear **Tsai–Wu failure criterion**. All primary carbon layers and custom wheel profiles returned a minimum **Reserve Factor RF** $\geq$ 1.0 across every load case, confirming that the aggressive mass reduction did not compromise structural safety margins.

4.4 Dissimilar-Material Interfaces and Joint Integrity

The CFRP-to-aluminium interfaces like suspension clevises and mounting brackets, present two failure modes that were addressed explicitly:

- **Galvanic corrosion.** A fibre-glass isolation layer is laminated between every carbon and aluminium contact surface, breaking the galvanic couple that would otherwise drive corrosion of the aluminium fittings over the vehicle's service life.
- **Joint loading.** Suspension clevis geometry and mounting positions were simulated under the per-lap load spectrum from the vehicle dynamics model with a **safety factor of 3**, confirming structural adequacy at all

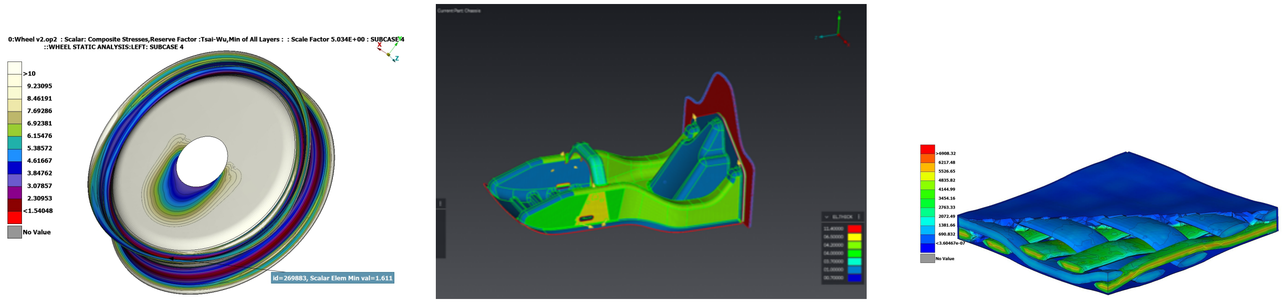

(a) Wheel Tsai–Wu failure-index distribution under the transient bump load case.

(b) Monocoque layer model.

(c) CFRP RVE model

Figure 8: Finite element validation of the primary structure (EPILYSIS solver, META post-processing).

attachment points before fabrication.

Together with the reduced peak loads from the suspension (Section 2), these measures allowed the average monocoque thickness to be reduced to 2.1 mm while preserving the durability required for repeated competition use.

5 Safety and Driver Ergonomics

5.1 Driver-First Packaging Methodology

Driver ergonomics were treated as a boundary condition on the vehicle geometry rather than a post-design check. Before the external surface was lofted, a digital driver model representative of the team's driver was positioned in CAD to define the minimum internal cockpit envelope: the volume required to seat the driver in a competition-legal posture while preserving full reach to all controls.

This envelope became a fixed input to the aerodynamic surfacing described in Section 1. Canopy height, windscreen rake, and cockpit width were set to the smallest values that cleared the driver model, resolving ergonomics and aerodynamics simultaneously: the driver package set the minimum frontal area, and the fuselage was lofted around it.

Human-factors design was not confined to the driver: the same posture-first reasoning was extended to the maintenance crew, whose working height and access are addressed in Section 6.

5.2 Cockpit Layout and Control Ergonomics

The cockpit was designed so that all primary interfaces (steering, braking, regeneration, and instrumentation) fall within the natural working arc of the seated driver without requiring the driver to adopt a compromised posture for any control operation.

(a) Cockpit view showing driver sightline over the nose.

(b) Custom CFRP and 3D-printed steering wheel with integrated regenerative braking paddle.

Figure 9: Cockpit environment and driver interface of Pyrforos IV.

Custom Steering Wheel and Regenerative Braking Interface

The steering wheel was fully designed and manufactured by the team, combining two materials to optimise mass, rigidity, and driver feel:

- **CFRP plate:** forms the structural backbone of the wheel, providing the torsional rigidity needed to transmit steering inputs precisely while contributing minimal rotational mass at the top of the steering column.
- **3D-printed components:** the dashboard/button carrier, handles, and regenerative braking paddle are additively manufactured, allowing complex ergonomic geometries at near-zero tooling cost.

The paddle integrates directly into the driver's natural grip position on the CFRP rim. When actuated, it sends a variable-level demand signal to the motor controller, modulating regenerative braking torque continuously rather than switching between fixed states. This allows the driver to recover kinetic energy to the battery during deceleration phases, particularly the approach to the mandatory compulsory stop, at a braking intensity precisely matched to the available distance and desired final speed. Friction braking handles full emergency stops; the paddle handles all routine deceleration, maximising energy recovery across the lap. The result is a driver interface where *every deceleration event is a charging event.*

The wheel's dual-material construction also reflects the team's broader manufacturing philosophy: CFRP where structural performance demands it, additive manufacturing where geometric complexity or iterability is the priority.

5.3 Reach, Posture, and Line of Sight

The CAD driver model was used to fix and verify the principal human-factors envelopes before manufacture; the measured values are summarised in Table 10.

Table 10: Measured driver human-factors envelopes (CAD driver model unless noted).

Parameter	Value	Basis
Horizontal field of view	210°	CAD eye-point sightline
Driver egress time	4.5 s (limit 10 s)	Timed: harnessed → clear
Accommodated stature range	150–180 cm	Digital human model
Seat back angle	32°	Cockpit package
Steering reach (elbow angle)	95–110°	Reach-arc verification

5.4 Safety Compliance

Pyrforos IV incorporates the roll-over protection, driver restraint system, firewall bulkhead, and structural safety provisions required by the Shell Eco-marathon technical regulations. All safety-critical load paths such as harness anchors, front hub under emergency braking, and monocoque floor under vertical impact, were explicitly included in the five-scenario FEA validation described in Section 4, confirming structural adequacy under worst-case conditions.

6 Sustainable Design and Manufacturing Practices

6.1 Sustainability as a System-Level Constraint

Sustainable practice in PIV was embedded as a design constraint across material sourcing, manufacturing process, and lifecycle design, rather than confined to material selection (Figure 10).

Reused
Transport container refitted from prior platform; tooling reused across generations

Repairable
78/109 parts (72%) spared; suspension, belt drive, 3D-printed controls

Recycled / Repurposed
CFRP offcuts → short-fibre steering plate; monocoque recycled at end of life

Locally Sourced
CFRP fabric, epoxy resin and foam core all sourced in Greece

Figure 10: Pyrforos IV lifecycle and sustainability summary, mapping each major design decision to its reuse, repair, recovery, or sourcing benefit.

6.2 Local Material Sourcing

All three primary structural materials (CFRP fabric, epoxy resin system, and structural foam core) were sourced from suppliers located in Greece. Local procurement reduced the embedded transport emissions associated with raw material delivery relative to international sourcing, and supported domestic industry.

The structural foam core also serves a dual sustainability function: as documented in Section 4, it substitutes panel depth for ply count in flat and low-curvature regions, directly reducing the volume of virgin carbon fibre consumed in the monocoque while simultaneously improving bending stiffness. Less carbon fibre used means less energy-intensive manufacturing at the fibre production stage.

6.3 Manufacturing Waste Minimisation

CFRP manufacturing typically generates two categories of waste: dry fabric offcuts and cured composite trim waste. PIV addressed both:

- **Ply nesting optimisation.** Fabric cutting patterns were nested carefully across each ply schedule to minimise dry offcut generation before lamination. No automated CNC cutting was available, making manual nesting discipline the primary waste-reduction lever at this stage.
- **Vacuum infusion process.** The monocoque was manufactured using a controlled vacuum infusion layup, which meters resin precisely through the dry fabric stack. This eliminates the excess resin inherent in hand wet-layup, reducing both resin consumption and the volume of resin-soaked waste consumables.
- **Offcut reutilisation: short-fibre compression moulding.** Cured and uncured CFRP offcuts were not discarded. Instead, they were chopped and consolidated using a short-fibre compression moulding process to produce structural parts where isotropic stiffness is acceptable and fibre continuity is not critical. The structural backbone plate of the custom steering wheel (Section 5) was manufactured by this method, closing a direct material loop between monocoque waste and a finished vehicle component.
- **Offcut collection for recycling.** All remaining CFRP offcuts not consumed by the short-fibre process were collected and segregated for mechanical recycling, shredding into short-fibre reinforcement feedstock. This diverts composite waste from landfill and returns material value to the supply chain, addressing the principal end-of-life challenge of thermoset CFRP structures.

6.4 End-of-Life Strategy for the CFRP Monocoque

Thermoset CFRP cannot be re-melted or conventionally recycled, and the team acknowledges this openly. Two end-of-life pathways have been defined for PIV's structure, in order of preference:

1. **Preservation and continued use.** PIV is intended to be retained as a reference vehicle in the team's collection, preserving the embodied energy and material value of the structure indefinitely and serving as a physical benchmark for future design generations.
2. **Mechanical recycling.** Should the structure reach the end of its serviceable life, the CFRP panels will be mechanically processed (shredded into short-fibre reinforcement) which can be reintroduced as a secondary composite feedstock. While this process does not recover fibre at its original length or strength, it is the currently viable industrial pathway for thermoset CFRP and represents a substantially better outcome than landfill disposal.

The team's position is that the most sustainable CFRP component is one that is never replaced: designing for longevity and multi-cycle use is a more effective strategy than designing for recyclability alone.

6.5 Component Repairability and Lifecycle Design

Repairability is also visible quantitatively in the configuration-controlled BOM (Table 3). Of the 105 tracked mechanical and structural part numbers, 78 (72 %) carry pre-defined held spares, and the entire suspension subsystem (30 of 30 parts) is spared and individually replaceable through the clevis mounting system (codes `PIV-SUS-01.04.xx`) without disturbing the monocoque. Designing the spare schedule into the part register at development time, rather than reacting to in-service failures, means a damaged component is restored from stock and its digital definition instead of triggering replacement of a parent assembly.

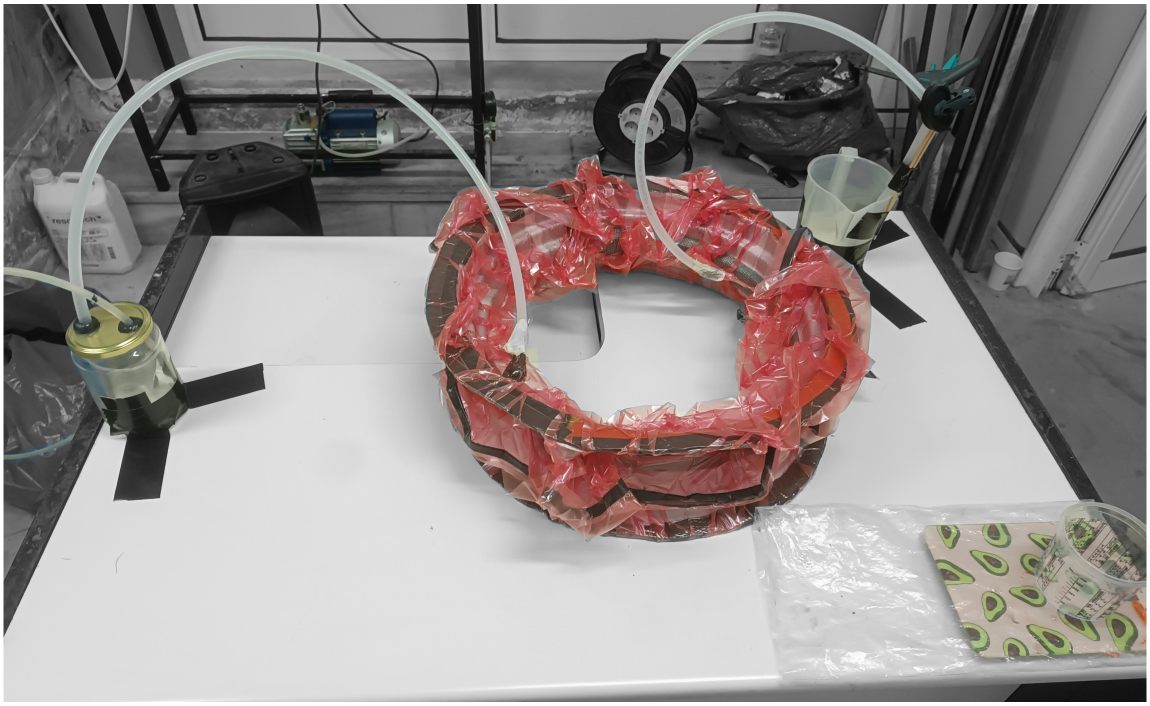

Figure 11: Vacuum infusion process of wheel rim.

- **Suspension components.** All double-wishbone and trailing-arm suspension elements are attached to the monocoque via the clevis mounting system described in Section 4. Individual components can be removed, repaired, or replaced without structural work to the chassis, preserving the monocoque across multiple competition seasons. The suspension system simultaneously extends chassis fatigue life by reducing peak transmitted loads, as established in Section 2.
- **Belt drive.** The 6:1 belt transmission is fully accessible and replaceable without structural disassembly, enabling routine drivetrain maintenance and belt renewal between competition attempts without removing or modifying the monocoque.
- **3D-printed steering wheel components.** The dashboard carrier, button holder, and regenerative braking paddle are additively manufactured. Any damaged or worn component can be reprinted from the original digital file at negligible cost, eliminating the need to replace the entire steering assembly and retaining the CFRP structural plate across the component's full service life.
- **Serviceability and access.** The full electronics suite is mounted to the rear bulkhead behind a removable tail fairing; with the tail detached, the entire bay is exposed for fault-finding and component replacement with no surrounding bodywork to work around, so diagnostics and repairs that would otherwise require partial disassembly are reached directly. All such work is carried out on a purpose-built elevating stand that raises the vehicle to standing working height, keeping the crew in a neutral posture and removing the repeated stooped manual handling that accelerates both component mishandling and operator fatigue.

6.6 Reuse Beyond the Vehicle: Transport Infrastructure

The team's transport container was not newly manufactured for this vehicle. The existing container from the previous platform was structurally modified and refitted to accommodate PIV's revised geometry. This decision avoided the material consumption and manufacturing energy associated with producing a new container, demonstrating that the team's lifecycle thinking extends beyond the vehicle itself to the full competition programme infrastructure.